Global Snow Cover Monitoring With Spaceborne K_u-band Scatterometer

Son V. Nghiem and Wu-Yang Tsai

***Abstract*—This paper presents a study to demonstrate the potential of a spaceborne K_u-band scatterometer to monitor global snow cover. Global K_u-band data were acquired by the National Aeronautics and Space Administration (NASA) Scatterometer (NSCAT) operated on the Advanced Earth Observing Satellite (ADEOS) from September 1996 to June 1997. NSCAT backscatter patterns over the northern hemisphere reveals boundaries between different snow classes, defined by the Cold Regions Research and Engineering Laboratory (CRREL), Hanover, NH, snow classification system at different times of the snow season. We show the evolution of the backscatter signature throughout the entire seasonal snow cycle. Within the snow extent determined by the National Oceanic and Atmospheric Administration (NOAA), Washington, DC, and Climate Prediction Center (CPC), operational snow product, K_u-band backscatter data expose detailed features and rapid changes as observed in *in-situ* snow depth data from surface weather stations in U.S., Canada, and Russia. Sensitivity of K_u-band backscatter to snow conditions is illustrated with the dramatic change over the U.S. northern plains and the Canadian prairie region corresponding to the snow event leading to the 1997 Flood of the Century. We discuss snow field experiments and data analysis plan to understand snow scattering mechanisms, to interpret snow backscatter, and to derive its relationship with snow physical parameters. In view of current and future satellite K_u-band scatterometers, the development of algorithms for quantitative snow cover monitoring is pertinent.**

***Index Terms*—Flood, Ku-band scatterometer, NSCAT, snow, snowmelt.**

I. Introduction

SNOW influences the global heat budget [1], [2] and has strong feedbacks with the planetary albedo and outgoing longwave radiation [3]. Snow cover is a significant climatic index [4] which can be used to predict and estimate the magnitude of recent changes in climate [5].

Temperature change in high latitudes is attributable to the albedo-temperature feedback process, and snow must be regarded as one of the key variables in the global change monitoring [6]. Different results from 17 general circulation models, varied from weak negative feedback in some models to strong positive feedback in others, indicate that snow feedback involves amplification or moderation caused both by cloud interactions and longwave radiation in addition to albedo effects of snow cover [7]. Global snow depth climatology, derived mostly from scheduled snow-depth observations, has been used in atmospheric general circulation and snow analysis models [8], [9].

Snow impacts a multitude of activities in engineering, agriculture, travel, recreation, commerce, and safety [10]. Snowmelt is an important water source for irrigation and drinking in many areas of the world [11], [12]. Heavy snow storms with rapid snowmelt in spring were accounted for the Flood of the Century in the Northern Plains causing loss of lives and several billion dollars in flood related damages [13]. In this regard, snow monitoring with a frequent coverage over regional scales is necessary for hazard prediction and mitigation.

Snow monitoring with satellite visible sensors, spaceborne microwave radiometers, and *in-situ* station observations has been summarized and compared to evaluate snow cover over the globe [6], [14], [15]. Satellite visible-band radiometers detect snow by its high albedo and dendritic signatures [16], [17]. Using Scanning Multichannel Microwave Radiometer (SMMR) data at 37 and 18 GHz, Chang *et al.* [18] developed retrieval algorithms for global snow covered area and snow water equivalent with 25 km to 50 km resolution, respectively. Grody [19] developed a decision-tree algorithm for snow cover mapping with a convolved resolution of 55 km from Special Sensor Microwave Imager (SSM/I) data at 19, 22, and 85 GHz. Synthetic aperture radar (SAR) data at C-band with high resolutions have been used to map snow cover and snowmelt [20]–[22]. Operational snow cover products, such as the NOAA National Environmental Satellite, Data, and Information Service (NESDIS) and Climate Prediction Center (CPC) snow extent [23], have been obtained from remote sensing data. Each type of sensor data has certain advantages and limitations.

For optical sensors, snow can be clearly detected due to large differences in albedo of snow cover (white) and bare ground areas (dark). An optical sensor typically has a large swath (2000 km or more) for snow monitoring on the global scale. Nevertheless, in vegetation covered regions such as boreal forests, the solar angle with respect to the horizon is low at high latitudes in cold regions. Trees block the view of the underneath surface and also cast long shadows on the snow cover. Such effects make the snow cover surface in forested areas look dark and the objective snow cover identification becomes difficult. During seasonal transitions such as snowmelt periods, clouds mask surface observations of snow and a long time period is needed to increase the chance of clear sky. Such observations are too long and sporadic to capture rapid changes of seasonal snowmelt transitions, which are important to both albedo-radiation effects and melt-water runoff.

Manuscript received September 6, 2000; revised June 19, 2001. This work was supported in part by the Jet Propulsion Laboratory, California Institute of Technology, Pasadena, under a contract with the National Aeronautics and Space Administration, and also by the 1999 Lew Allen Award of Excellence.

The authors are with the Jet Propulsion Laboratory, California Institute of Technology, Pasadena, CA 91109 USA (e-mail: nghiem@solar.jpl.nasa.gov).

Publisher Item Identifier S 0196-2892(01)08833-7.

A passive radiometer also has relatively a large swath and can see through clouds. An important advantage of passive radiometers is that a record of several decades of data has been collected allow long-term studies of climatic trends. A radiometer measures brightness temperatures (product of emissivity with physical temperature) by the natural radiation emitted from the medium to the radiometer antenna. Inherently, one-way antenna is applied and the measurements typically have low resolutions. For snow detection, novel algorithms such as Grody's [19] objectively exploit the dispersion of snow at different SSM/I frequencies. However, the use of multiple-frequency radiometer data forces the results to a lower resolution (55 km) because of the low frequency (19 GHz) and to a higher susceptibility to atmospheric effects at the high frequency (85 GHz).

Compared to radiometers, a SAR has a resolution (as high as several meters) higher by several orders of magnitude. High-resolution data are necessary to resolve the hillslope scale (less than 100 m) for hydrologic applications at small scales. A microwave SAR also has the capability to see through clouds and darkness. However, with current satellite SAR technologies, a high-resolution SAR typically has a very small swath (50 km to 500 km) and requires a very high data rate. Consequently, SAR results are subject to small local areas with an infrequent coverage (several days to a week) and/or a fragmented coverage with missing-data areas interlacing with data-covered areas. Furthermore, the incidence angle is varied from small to large values across the swath. At each pixel, the measurement is at one incidence angle and the variability in incidence is embedded in the data making snow algorithms more complicated and less accurate.

In this paper, we investigate the sensitivity of K_{u}-band backscatter to snow properties, and demonstrate the potential use of a spaceborne K_{u}-band scatterometer to monitor global snow cover. Spaceborne scatterometers launched by NASA include Seasat scatterometer operated at 14.6 GHz, NSCAT at 14.0 GHz (13.995 GHz to be more exact), and SeaWinds at 13.4 GHz. All of these spaceborne-scatterometer frequencies are in the K_{u} band (which starts at 12 GHz), and we use the term K_{u} band to indicate these frequencies. Similar to other microwave sensors, the K_{u}-band scatterometers can make surface observations through cloud cover and darkness as opposed to optical sensors. A scatterometer typically has a larger swath (up to 1800 km for SeaWinds) for a much large and frequent coverage compared to SAR. The resolution is typically better than a radiometer but coarser than SAR resolution. Compared to brightness temperature, scatterometer signatures are strongly sensitive (to be presented later in the paper) to wetness in snow and can be used to detect early snowmelt.

Based on scattering physics and measured radar data, we study K_{u}-band backscattering response to snow compared to that at other frequencies, and discuss advantages of the K_{u}-band scatterometer. Then with NSCAT data, we show the K_{u}-band backscatter response over snow covered regions with different snow types in the northern hemisphere in conjunction with the NOAA/NESDIS and CPC snow extent product throughout the 1996–1997 snow season. We use *in-situ* snow depth data from surface weather stations in U.S., Canada, and Russia to compare with changes in NSCAT backscatter and with changes in NOAA/NESDIS and CPC snow extent. To illustrate the sensitivity of K_{u}-band backscatter to snow conditions, we show the dramatic change over the U.S. northern plains and the Canadian prairie region corresponding to the snow event leading to the 1997 Flood of the Century. We also point out limitations of NSCAT data for snow applications. Finally, we summary the paper and discuss future developments for global snow monitoring with K_{u}-band scatterometers.

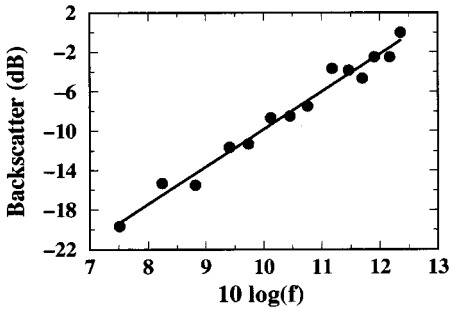

Fig. 1. Backscatter at 50° incidence angle and horizontal polarization as a function of frequency for dry snow. Data [25] are plotted with black dots and the continuous line represents the linear regression. The horizontal axis is for $10\log(f)$ from 7 to 13 corresponding to the frequency range from about 5 GHz to 20 GHz.

II. Physical Principles

A. Snow Scattering and Frequency Response

Snow grain sizes range mostly in submillimeter and millimeter scales, except that depth hoar crystals can develop to centimeter scales typically in a subsurface snow layer. For a snow grain much smaller than the electromagnetic wavelength, the scattering follows the Rayleigh scattering law [24], and the backscattering cross-section is given as

$$\sigma_s = 64\pi^5 \left(\frac{\epsilon_s - \epsilon_0}{\epsilon_s + 2\epsilon_0}\right) a^6 f^4 \tag{1}$$

where

- ϵ_s permittivity of ice scatterers;
- ϵ_0 permittivity of the air background;
- a snow grain radius;
- f electromagnetic wave frequency.

According to the Rayleigh scattering (1), the backscatter is proportional to the fourth power of the wave frequency. Taking 10 times of the base-10 logarithm of both sides of (1), we obtain backscattering coefficient σ_0 in the decibel (dB) domain as

$$\sigma_0(\mathrm{dB}) = A(f) + P[10log(f)]. \tag{2}$$

In (2), coefficient $A(f)$ is a weak function of frequency f due to the dispersive characteristics of ϵ_s, and P is the power index. For Rayleigh scattering, $P = 4$.

Radar measurements of dry snow for the horizontal polarization at 50° incidence angle [25] show that backscatter agrees well with the Rayleigh-scattering law over the range of frequency from C-band to K_{u} band as shown in Fig. 1. The total snow depth was 26 cm with different densities at different depths (denser for upper snow), snow water equivalent was 5.9 cm, and snow temperatures were as cold as -13 °C at the top layer and -1 °C at the frozen soil [25]. The dots represent measured

data by Stiles and Ulaby [25], and the continuous curve is the linear fit with the form of (2). The regression analysis shows that $P = 3.81$ (within 5% of $P = 4$ for Rayleigh scattering) with a very high correlation coefficient of 0.988. An important indication of these results is that snow backscatter at $K_{\rm u}$-band around 14 GHz is 5.4 times stronger than that at X-band 9 GHz, and more than 40 times stronger compared to that at C-band 5.3 GHz for $P = 3.81$. This is consistent with results from radar experiments of seasonal snow indicating that dry snow has very little influence on backscatter at frequencies up to 10 GHz [26]. In this respect, a higher-frequency radar is better to detect snow. However, when the frequency is so high such that the Rayleigh scattering condition is not satisfied and multiple interactions among the snow grains also becomes significant, the dispersive scattering loss is important and the backscatter can only increase with a smaller power index compared to the forth-power relationship in the frequency dependence. Experimentally, data by Stiles and Ulaby [25] show a modest increase by about 3 dB between 16.6 GHz to 35.6 GHz. Theoretically, the dense medium model or strong fluctuation theory (discussed in the next section) is more applicable for multiple scattering effects.

B. Snow Attenuation and Saturation Effects

While electromagnetic waves at higher frequencies have a stronger response to snow scattering, wave attenuation needs to be considered. Wave propagation and attenuation in a scattering medium are characterized with a complex effective permittivity tensor $\overline{\overline{\epsilon}}_{eff}$. Under the strong permittivity fluctuations theory, the permittivity tensor is given in the form of [27]

$$\overline{\overline{\epsilon}}_{eff} = \overline{\overline{\epsilon}}_{g} + \epsilon_0 \overline{\overline{\xi}}_{eff} \tag{3}$$

where $\overline{\overline{\epsilon}}_{g}$ is the effective permittivity tensor in the quasistatic limit, which is reduced to the Polder-van Santen dielectric mixing, and $\overline{\overline{\xi}}_{eff}$ is the effective scatterer related to the scattering effects on wave speed and attenuation. Detailed expressions of $\overline{\overline{\epsilon}}_{eff}$ for inhomogeneous anisotropic media with multiple nonspherical scattering species have beed derived and presented [28], [29]. Both absorption loss and scattering loss are accounted for in (3). A scattering medium such as snow is inherently dispersive and the wave attenuation is more severe at higher frequencies. Because of the attenuation, backscatter from snow cannot increase further and becomes saturated after a certain snow depth where the waves cannot reach.

The saturation effects in backscatter for the horizontal polarization at 57° incidence angle are shown in Fig. 2. Results at 9 GHz and at 16.6 GHz are from empirical model functions, relating backscatter to dry snow water equivalent (SWE), derived with measured data [30]. SWE is defined as the integration of snow density over snow depth. Because there are no measured data to determine the model function at 14 GHz, we use the linear relationship between snow backscatter versus the logarithm of frequency as presented above to interpolate the results between 9 GHz and at 16.6 GHz to obtain the $K_{\rm u}$-band backscatter. Fig. 2 indicates that backscatter has a good increasing trend at 9 GHz, and starts to become less sensitive to large values of SWE at 14 GHz. Note that SWE for the results

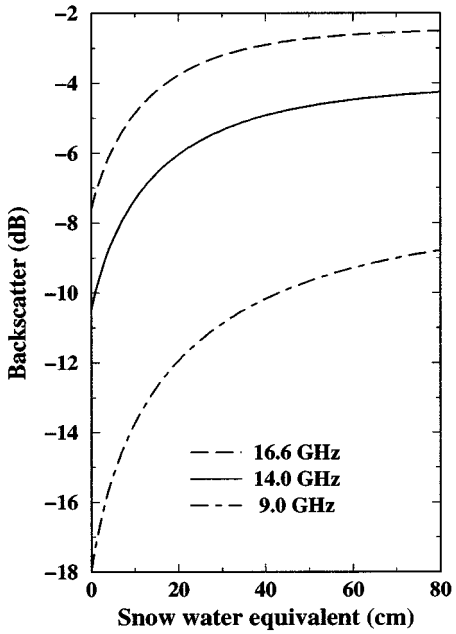

Fig. 2. Backscatter at 57° incidence angle and horizontal polarization as a function of snow water equivalent for dry snow. The curves for 16.6 GHz (dashed curve) and for 9.0 GHz (dash-dotted curve) are from empirical model functions [30]. The continuous curve is for 14.0 GHz derived by the interpolation in the logarithmic frequency domain from the empirical results at 9.0 GHz and 16.6 GHz.

in Fig. 1 is 5.9 cm, which is in the regime well below the SWE at which saturation effects become important. At 16.6 GHz, the backscatter changes only about 0.7 dB for the range of SWE from 30 cm to 80 cm due to the saturation effects. Thus, a frequency lower than 16.6 GHz is more desirable to detect thicker snow depth.

With the aforementioned considerations, a $K_{\rm u}$-band scatterometer system is applicable to snow monitoring. A lower frequency radar has a much weaker snow backscatter response that is harder to detect thinner snow, and is contaminated by more radar-system noise due to a lower signal-to-noise ratio. For example, C-band backscatter for the snow case of Fig. 1 is about -20 dB [25], which can be below the noise floor of high-resolution SAR measurements. Also at C-band, backscatter due to vegetation is stronger and can significantly contribute to the total backscatter or even dominate the snow signature. At Ku band, snow backscatter is strong and is not masked by forests (to be presented in Section II-B and Section III-C below). A higher frequency radar is limited by the saturation that causes great difficulties in detecting thicker snow depth.

Furthermore, a high relative accuracy is necessary to determine snow water equivalent (SWE). For example, a relative calibration accuracy of ± 1 dB for one standard deviation (1σ) at the mean backscatter value of -10 dB still results in a large uncertainty in over a wide range of SWE from 30 cm to 80 cm even for the case of 9 GHz with the least saturation effects for the different frequencies shown in Fig. 2. Spaceborne $K_{\rm u}$-band scatterometers have been demonstrated to have an excellent relative accuracy of ± 0.3 dB at three standard deviation (3σ) for NSCAT [31] or, even better, ± 0.2 dB for SeaWinds [32], which can provide accurate measurements to retrieve SWE.

C. Effects of Vegetation Cover

Vegetation cover such as boreal or taiga forests occupies a large part of cold land regions. The forest penetration is shallower at higher microwave frequencies for a continuous vegetation coverage such as the dense foliage canopy in tropical rain forests. For forests over winter cold land, the vegetation cover is not continuous. In fact, it has large gaps among separated coniferous trees or deciduous trees without leaves. In this case, the gap model for the vegetation cover should be more representative rather than the continuum model. A higher frequency f corresponds to a shorter wavelength $\lambda = c/f$ where c is the speed of light in air. At 14 GHz, the wavelength is $\lambda = 2.1$ cm and gaps larger than that can allow K_{u}-band waves to go through.

If the vegetation cover dominates the total backscatter, then backscatter pattern should be distinctive over very different vegetation regions such taiga and tundra, and their boundary should be observable particularly when there is no snow cover. Moreover, during the winter season, if the vegetation cover continue to dominate the total backscatter masking out snow backscatter signatures, then the backscatter should stay relative constant because the vegetation is in the dormant state without growth. Also, the temperature is low in cold winter and free water in trees is minimized due to biophysical mechanisms such as xylem hydraulic conductivity reduction or xylem embolism [33]–[35]. Consequently, tree effective permittivity is low and stable, and backscatter from the vegetation is weaker.

On the other hand, if the frequency is high enough so that the radar cross section (RCS) from snow is higher than the vegetation "RCS floor," then the backscatter should increases for a thicker snow accumulation during the cold winter. Depending on the operating frequency, the radar data have to exhibit the increasing trend of snow accumulation during the cold winter over both forested and exposed areas as an indication of the backscatter response to snow in order to have a potential for snow applications. This serves as a basis to determine an appropriate operational frequency for radar remote sensing of snow.

D. Backscattering Mechanisms and Seasonal Evolution

Seasonally, time-series backscatter of snow should follow a definitive trend corresponding to the seasonal evolution of snow. To examine the trend, consider all the volume and surface scattering mechanisms depicted in Fig. 3. The total backscatter over the landscape within the radar footprint consists of: (1) scattering due to rough surfaces, (2) direct scattering from volume scatterers such as snow and vegetation, (3) scattering of reflected waves, (4) reflection of scattered waves, and (5) double reflected scattering. Detailed expressions of the these terms in the calculation of the total backscatter from multilayered inhomogeneous isotropic and anisotropic geophysical media have been derived and presented elsewhere [28], [29], [36]–[38].

From fall going into early winter, term (1) for rough surface decreases as the soil changes from thaw to freeze stage causing a significant decrease in soil effective permittivity and consequently the decrease in rough surface scattering. The four-volume scattering terms (2–5) also decrease during the fall-winter transition because the tree permittivity decreases due to the free water decrease in tree (direct volume scattering term),

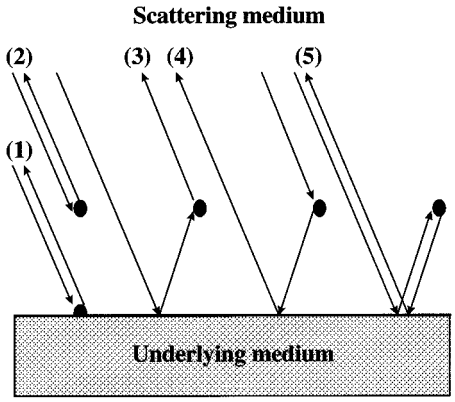

Fig. 3. Scattering mechanisms: (1) direct scattering due to rough surface, (2) direct scattering from volume scatterers, (3) scattering of reflected waves, (4) reflection of scattered waves, and (5) double reflected scattering.

and because the soil reflectivity decreases in the freezing stage (reflection-scattering interaction terms). The overall decreasing trend holds true for the different microwave frequencies since all scattering mechanisms follows the decreasing trend over the seasonal transition.

As snow arrives and accumulates during the winter, the backscatter increases if the radar frequency is high enough to have a strong response from snow. At low frequencies, backscatter is dominated by vegetation and stays unchanged during the cold winter as discussed above. By the end of the snow season, the total backscatter decreases precipitously (due to lossy wet snow) with strong diurnal effects during the snowmelt process, which is usually within one or two weeks from the onset of snowmelt. As the season transitions from winter into spring, the landscape thaws up, soil and tree permittivities increase, the reflectivities increase, and all the scattering terms increase resulting in the increase of the total backscatter.

Thus, the seasonal trend of global snow backscatter signature has the characteristics: (1) low backscatter before snow arrival, (2) gradually increasing backscatter during the cold winter season corresponding to more snow accumulation, (3) rapidly decreasing backscatter be the end of the snow season as snowmelts, and (4) backscatter is increasing again as snow departs. These trends of snow backscatter should be observable from seasonal global data measured by NSCAT if the backscatter does come from snow. This suggests that time-series backscatter data are appropriate for snow monitoring since snow accumulation and snowmelt are temporal processes.

E. Snow Wetness Effects and Melt-Freeze Cycles

In wet snow, the liquid water phase has a large imaginary part representing a large absorption loss in the first term in (3). Furthermore, the large value of liquid water permittivity leads to a strong scattering loss in the second term in (3). Thus, the wetness in snow causes a strong increase in the total wave attenuation and consequently a large decrease in the backscatter from the snow pack. At K_{u} band, backscatter can decrease more than 5 dB for 3% wetness [25]. Such a strong sensitivity to the liquid water content in snow is excellent for a radar to identify wet and dry snow and to estimate the snow wetness. This is important to

detect early snowmelt conditions for applications to flood forecasting.

Snow wetness is governed by the thermal condition of the snow pack. Fluctuations in air temperatures and diurnal effects cause significant changes in snow wetness. Diurnal effects have been used to delineate snowmelt zones over the Greenland ice sheet [39]. Thus, superimposed on the above general seasonal trends of snow backscatter are fluctuations such as transient temperature variations causing short-term backscatter fluctuations. Higher temperatures and solar radiations in spring time can increase snow wetness in the top layer, leading to a strong decrease in backscatter at K_{u}-band 14 GHz, while the landscape is still fully covered by snow. The snow pack can refreeze and the backscatter can rebound as the temperature becomes cold again. Thus, the strong backscatter change is inversely related to temperature changes during the melt-freeze cycles.

While a temperature increase over snow leads to a backscatter decrease, a temperature increase thawing the landscape without snow leads to a backscatter increase. This is due to increases both in surface scattering due to the higher soil permittivity and in volume scattering due to the higher reflections and higher scatterer permittivities. Wismann [40] showed that changes in C-band backscatter are similar between two completely different cases: one with snow cover and freezing temperature, and the other with ground thawing with temperature well above freezing (see Fig. 3 of the reference [40]). Therefore, a change in backscatter should not be interpreted as an extensive land thaw without considering the trend and the sign of the backscatter change.

In view of the above physical principles, we investigate K_{u}-band backscatter over snow covered regions to examine its spatial distribution and its temporal evolution over the snow season to be presented in the following sections. It is necessary to show that the backscatter signature exhibits strong changes over snow covered regions with spatial characteristics and seasonal variations corresponding to different snow properties and seasonal snow processes to demonstrate the potential use of the spaceborne scatterometer for global snow monitoring.

III. Backscatter Patterns Over Snow Classes

A. Global Snow Classes

Based on physical characteristics, global seasonal snow is classified into six classes: *1) tundra, 2) taiga, 3) prairie, 4) alpine, 5) maritime, and 6) ephemeral or no snow* according to the CRREL snow classification system [41]. In addition, perennial ice such as the Greenland ice sheet is grouped into a class called *ice*. Each of the snow classes is defined by a unique ensemble of texture and stratigraphy including snow layers, thickness, density, crystal morphology, and grain characteristics. Sturm *et al.* [41] have described physical characteristics of the snow classes and presented data on their depth range, bulk density, and layer number.

Some of the snow class names, retained from historic snow classification developments, are not necessarily associated with a particular vegetation type, and thus a tundra snow cover can exist over a region with no tundra [41]. The snow class data base is available over the Northern Hemisphere with a $0.5^\circ \times 0.5^\circ$ grid in latitude and longitude, the global snow class distribution is presented in Fig. 4(a) with the above numbering for different snow classes and number 7 denotes the perennial ice class. An important advantage of the CRREL snow classification system is that it helps to infer more information about the snow cover compared to using remote sensing data alone; this is possible because different snow classes have definitive ensembles of physical characteristics [41].

B. Global NSCAT Backscatter Data

The National Aeronautics and Space Administration (NASA) Scatterometer (NSCAT) was operated at about 14 GHz on the Advanced Earth Observing Satellite (ADEOS) from September 1996 to June 1997. NSCAT had double-sided swaths, each with a coverage of 600 km spanning a range of incidence angles within 10° to 70°. On each side, there were three beams with the vertical polarization and one beam with the horizontal polarization on each side. The relative accuracy of backscatter measurements was estimated about 0.3 dB, and further information on NSCAT system and calibration has been reported by Tsai *et al.* [31].

In this paper, we use the vertical polarization data because there were more data at that polarization. The NSCAT backscatter resolution was approximately 7 km $\times$ 25 km on the ground and the data were binned into 25-km cells. In each cell, there are typically several backscatter data points at different incidence angles. To account for the incidence angle variations, we use the data within a given cell to calculate the slope versus incidence angle and interpolate the measurements to a fixed incidence angle at 45°.

In general, the backscatter in the decibel domain is a nonlinear function of incidence angle. At small incidence angles, the scattering from rough surface can be dominant giving rise to a steeper slope. In the larger range of incidence angles where backscatter is dominated by volume scattering, the slope is shallower. At very large incidence angles, backscatter is weak and measurements are noisy. To obtain a consistent global data set for snow applications, we eliminate data at small and large incidence angles and retain data within 30° to 60° before carrying out the interpolation to 45°. Furthermore, we test this approach by using data within $45^\circ \pm 10^\circ$ for the interpolation and compare with the interpolated results using data within $45^\circ \pm 15^\circ$ (30° – 60°). No significant differences were found and thus data within 30° – 60° can be used to obtain NSCAT images at a uniform incidence angle of 45°. The price for the data set with a uniform incidence angle is the reduction in coverage because the entire swath cannot be utilized.

C. Comparison of Backscatter and Snow Class Distribution

If K_{u}-band backscatter has a strong response to snow physical properties such as snow depth, density, grain size [sixth power of size according to (1)], and wetness, the backscatter patterns should reveal some correspondence to different snow classes. To compare the backscatter patterns with the global snow class distribution, we overlay the snow class contour on NSCAT backscatter maps at different times of the winter as presented in Figs. 4(b)–(e).

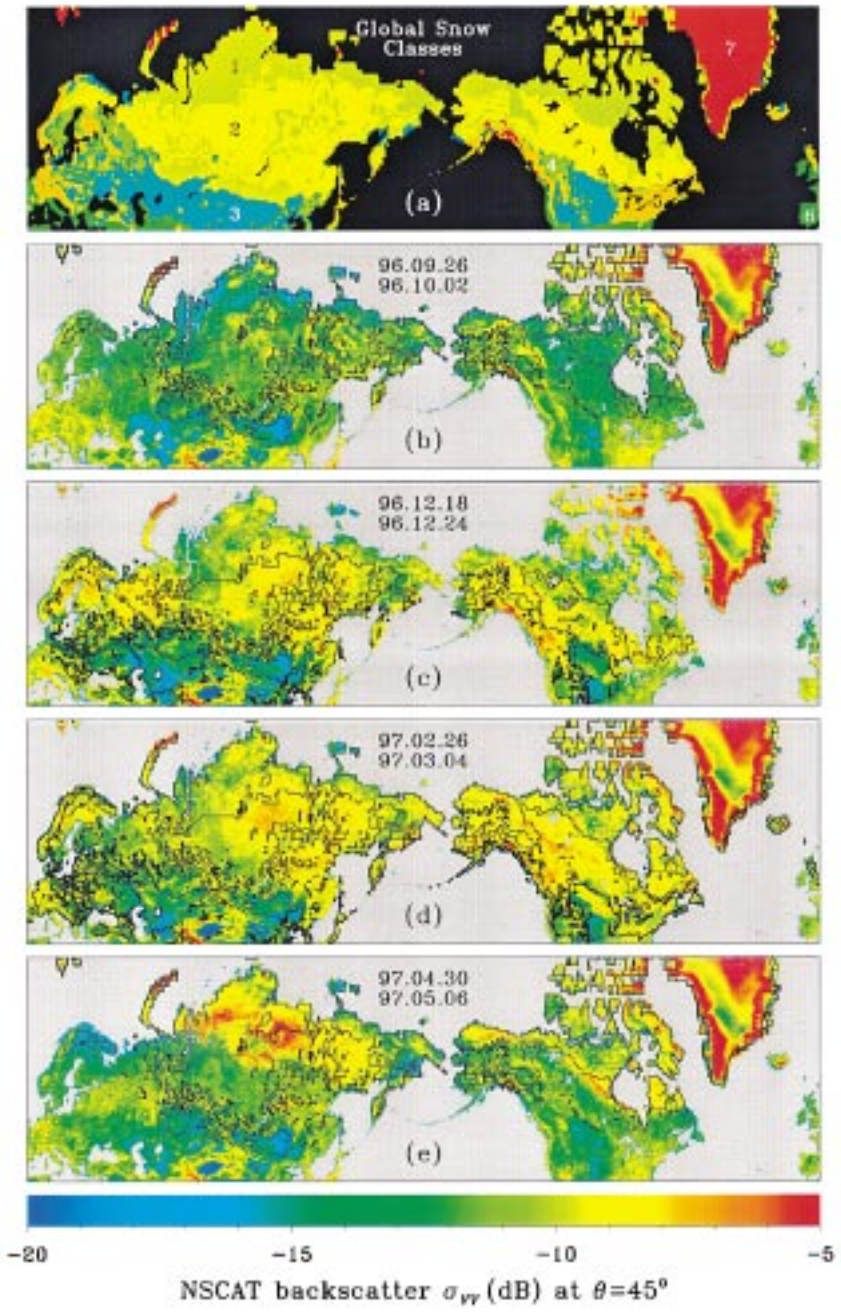

Fig. 4. Comparisons of backscatter patterns with global snow classes: (a) global snow classes [38] denoted with 1 for tundra, 2 for taiga, 3 for prairie, 4 for alpine, 5 for maritime, 6 for ephemeral or no snow, and 7 for perennial ice, (b) comparison of NSCAT backscatter pattern for the period from 26 September to 2 October 1996 with overlaying contours for tundra snow and perennial ice classes, (c) comparison for the period 96–12-18 to 96–12-24 with contours for prairie and taiga snow classes, (d) comparison for the period 97–02-26 to 97–03-04 with contours for tundra, maritime, and prairie snow classes, and (e) comparison for the period 97–04-30 to 97–05-06 with contours for tundra snow and perennial ice classes.

Fig. 4(b) shows NSCAT backscatter in late September to early October 1996 when much of the northern hemisphere was not covered by snow. In Fig. 4(b), we overlay the contours for tundra snow and ice classes. An interesting observation from Fig. 4(b) is that no distinction in backscatter is seen across the boundary between taiga forest and tundra regions located over the Canadian Shield [42] extending from Labrador/Newfoundland in the east up to the Northwest Territories in the west side of Canada. The lack of differences in backscatter over two very different vegetation regimes indicates the insensitive response of K_{u}-band scatterometer measurements to vegetation at high latitudes. This observation from NSCAT data verifies that the vegetation backscatter does not dominate the total backscatter from the cold-region landscape as we discuss in Section II-C.

There were some limited snow covered areas at high latitudes at the time of Fig. 4(b). A high backscatter area appears in red is noted in the region of St. Elias Mountains in the south-east part of Alaska extending into the south-west corner of the Yukon Territory in Canada. This area is characterized by high elevation terrain including Mt. Logan, the highest in Canada, where perennial snow/ice cover is observed. Comparing Figs. 4(a) and (b), we note that this area is exactly enclosed by the contour of

the ice class (class 7). In the north of Alaska, the southern extent of a yellow area representing backscatter around -8.5 dB is very well coincident with the boundary of between tundra and taiga snow classes. Also noticeable is the yellow feature seen from the middle east part on Alaska protruding through the Yukon Territory. At that time, no systematic pattern is obvious over the Eurasian region.

Fig. 4(c) presents backscatter patterns, with overlaying contours for prairie and taiga snow classes, during the winter week before Christmas eve in 1996. In the U.S. northern plains and the Canadian prairie, excellent distinctions between prairie snow and other snow classes including taiga snow over the north side, alpine snow in the east and the west sides, and maritime snow in the west part of US. NSCAT backscatter backscatter patterns in this north American region and the snow class boundaries are well correlated given that the global snow classes were derived based on long-term climatology data [41]. Over the northern Canada and Alaska, the boundary between tundra and taiga snow classes became apparent with stronger yellow backscatter for taiga snow compared to weaker light-green backscatter for tundra snow. Across the east-west extent of Eurasia from northeastern China, through Mongolia and Kazakstan, to eastern Europe, NSCAT backscatter patterns correspond to the taiga snow class in the north side and other snow classes in the south side.

Later into the winter season, backscatter patterns in February-March 1997 are plotted in Fig. 4(d) with overlaying contours for tundra, maritime, and prairie snow classes. Compared with the earlier backscatter images in Figs. 4(b) and 4(c), the increasing trend of backscatter for more snow accumulation at this later time in the winter season is evident not only over tundra regions but also over taiga forests. This result has an important implication that snow backscatter signatures are not masked by the vegetation cover, and thus demonstrates the potential use of K_{u}-band scatterometer for remote sensing of global snow cover as discussed in Section II-C. Over much of the north American continent, the backscatter distinction across the boundary between tundra and taiga snow class disappeared except over the Northwest Territories. A significant part of the north American prairie snow region was also filled up with a stronger yellow backscatter pattern. Along the west coast of US and Canada, the long stretch of maritime snow corresponded to an elongated strong backscatter appeared in orange, which was also observed in Fig. 4(c). A stronger yellow backscatter pattern became more apparent over the maritime snow in the European region above Italy. However, over much of Eurasia, backscatter patterns were complicated and were not well correlated with the snow class distribution pattern.

Corresponding to the late stage of the snow season, Fig. 4(e) with overlaying contours for tundra snow and ice classes shows several interesting backscatter patterns. The backscatter boundary between tundra and taiga in Alaska and Canada reappeared with a reverse backscatter pattern: the backscatter over tundra snow was stronger compared to that over taiga snow especially over north Alaska and Labrador, Canada, which is the opposite of the case in December shown in Fig. 4(c). The feature over the tundra snow from Alaska protruding into Yukon Territory also became evident again as in the September-October case in Fig. 4(b). At this late snow season, the ice class was still observable as a red area in the St. Elias Mountains. Another ice class region in red was also found throughout the season in the north of the Novaya Zemlya island between Barents and Kara Seas. Over Europe, much of the snow cover was departed; however, the northern and eastern Siberia still had strong backscatter patterns. In the west Siberia, this pattern appeared to stay in the taiga snow regions in Yakutia and Magadan. In northern Siberia, strong yellow-red backscatter spanned over both tundra and taiga snow classes.

Overall, we found NSCAT backscatter patterns correlated well with the snow class distribution in America but not quite as well over Eurasia. This is not surprising because the initial snow class map validation by Sturm *et al*. [41] indicates an excellent agreement of 90% in Alaska while the agreement in the former USSR is only 62%.

IV. Backscatter Evolution Over Snow Cover Regions

A. NSCAT Backscatter Images

To study the seasonal evolution of NSCAT backscatter over snow cover regions, we process NSCAT data to obtain global backscatter images at the vertical polarization and 45° incidence angle over the entire 1996–1997 snow season. Because only subswaths of NSCAT data can be used as discussed in Section III-B, one full global image requires one week of data for a complete coverage. The results from weekly NSCAT data are presented biweekly in 18 images in Figs. 5(a)–(r). Note that there are missing data over the western US from October 1996 to February 1997 as seen in Figs. 5(c)–(k). This was due to radar calibration activities with a ground calibration station located at White Sands, New Mexico [31], [43].

B. Snow Cover Extent

To provide an indication of snow cover areas, we use the NOAA/NESDIS and CPC snow extent product [23]. The operational snow cover data are hand derived from satellite data, primarily from the Geosynchronous Operational Environmental Satellites (GOES), the Advanced Very High Resolution Radiometer (AVHRR), and the European weather observation satellite METEOSAT [44]. The snow extent data are gridded in an 89×89 array overlaid on a polar stereographic projection with 1 and 0 representing snow or no-snow respectively. Snow extent data are converted into a $2^\circ \times 2^\circ$ grid in latitude and longitude, and then plotted as contours over the weekly NSCAT images at the same time periods as shown in Figs. 5(a)–(r). Note that most of the missing data area in the western US did not locate in the snow extent contours during the NSCAT calibration period as seen in Figs. 5(c)–(k).

C. Seasonal Trends

As observed in the time series of NSCAT images in Figs. 5(a)–(r), the temporal evolution of backscatter signature within the northern hemispheric snow cover regions does exhibit the seasonal characteristic trend of snow backscatter response as discussed in Section II-D. At the beginning of the snow sea in early October 1999, the backscatter within the snow extent contours was low. The backscatter became stronger

(more yellow and red) and the regions of strong backscatter was expanding as the snow cover extended further south as the snow season progressed. In the peak period of the season from late December 1996 to late February 1997, the strong backscatter pattern was reaching a maximum extension corresponding to the maximum extent of the NOAA/NESDIS and CPC snow product. In March 1997, the yellow backscatter area started to reduce. In late March and early April 1997, the high backscatter pattern was rapidly decrease. By May, this pattern was already limited to very high latitudes and mostly departed in June. These trends in the backscatter signature provide another evidence of the sensitivity of K_u-band backscatter in response to the seasonal snow evolution over the northern hemisphere.

As an aside note, in middle and low latitude regions outside the snow extent, there were also high backscatter areas such as the temperate regions in eastern U.S. and in China. The backscatter trends in these regions, dominated different terrain types, either remained relatively unchanged or did not follow the characteristic seasonal backscatter signature of snow.

D. Regional Trends

In snow cover areas, NSCAT backscatter revealed different details during the seasonal evolution over different regions of the world. In the US northern plains and the Canadian prairie regions, the prairie snow area appeared to be filled in from the south leaving a shrinking weak backscatter pattern in the middle [Fig. 5(d)–(i)]. Strong backscatter response to snow started first in Alaska and western Canada corresponding to earlier arrival of snow in this region. The Labrador and Newfoundland regions had stronger backscatter response to snow later in the season. Toward the end of the snow season, the high backscatter pattern in north America retreated to the north more rapidly compared to the NOAA/NESDIS and CPC snow extent retreat.

In Eurasia, strong backscatter response to snow appeared first in east Siberia corresponding to earlier snow arrival in this region [Fig. 5(a)–(c)], which has a high topography. A high backscatter band within the strip of snow extent contour was observed along the region of the Stanovoy and Yablonovyy ranges in the middle of east Siberia. Until early December [Fig. 5(e)], the strong backscatter pattern was limited to the east of the Ob River. However, later in December and until February, the backscatter responded strongly to snow spanning the entire northern Siberia and Europe.

In the late snow season, both the backscatter pattern and NOAA/NESDIS and CPC snow extent indicate snow retreat from the west in Europe moving toward the east into Siberia. In east Siberia, the general trend was that snow retreat started from the south moving northward and eastward as observed by NSCAT backscatter in agreement with the trend in the NOAA/NESDIS and CPC snow extent product. With the reduction from the west and from the south, snow cover became more and more isolated back to the northeast of Siberia. However, NSCAT backscatter revealed more details within the NOAA snow extent contour. For instance, the high backscatter pattern already reduced to Yakutia and the east as observed in Figs. 5(n)–(o) in April 1997 while the NOAA snow extent was still covering much of Siberia.

V. Comparison With In-Situ Snow Depth

NSCAT backscatter exhibited rapid changes within the snow extent during the seasonal transition. This is clearly observed in Fig. 5(m)–(r) over the northern hemisphere. As discussed in Section II-D, such rapid backscatterer changes are due to the sensitive response to the typical fast snowmelt process. To examine this relationship, we compare NSCAT backscatter patterns with *in-situ* snow depth together with local temperature measurements. *In-situ* meteorological parameters, measured at global weather stations, are obtained from the NOAA National Climate Data Center [45]. We carry out the comparison over three important snow-covered regions of the world: Alaska in U.S., Ontario in Canada, and Siberia in Russia. NSCAT backscatter are plotted in Fig. 6(a)–(c) over these regions in the April transition periods together with the NOAA snow extent and weather station locations.

A. Alaska

NSCAT backscatter over Alaska during 23–29 April 1997 in Fig. 6(a) reveal an interesting pattern with lower values in the middle sandwiched between high backscatter regions in the north and in the south. This pattern suggests an earlier snowmelt in the middle internal region of Alaska. At that time, snow still covered the northern region because of lower temperatures at the higher north latitudes. In the south of Alaska, the later snow departure was due to the thicker snow cover over higher altitudes of the southern local topography.

To verify the relationship of Alaskan NSCAT backscatter signature with the seasonal snow characteristics, we obtain *in-situ* data from three different stations spanning over the north-south dimension of Alaska: Umiat located at 69° 22'N and 152° 08'W with an altitude of 85 m, Fairbanks at 64° 49'N and 147° 52'W and 138 m, and Paxson at 63° 02'N and 145° 30'W and 809 m. *In-situ* snow depth and air temperature data are plotted in Fig. 7(a)–(d) for the above three stations, respectively. The time period corresponds to the NSCAT image in Fig. 6(a) for this case study is marked with the vertical thin lines in Fig. 7. The typical trend of the snow cover observed at these stations in Alaska shows a gradual accumulation with a gradual increase in snow depth through the snow season and then a rapid decrease of snow thickness due melting in the spring time.

Specifically, at the time period of NSCAT observations shown in Fig. 6(a), Umiat station still had 50-cm snow cover while the maximum air temperature started to reach to above freezing with the mean temperature still well below freezing as seen if Fig. 7(a). At Fairbanks station, the snow cover was melting and the snow depth decreased rapidly from more than 50 cm at the beginning of April to virtually no snow by the end of April. This fast snowmelt was due to a significant warm spell in the first half of April with a short refreezing period in the middle of April followed by the spring thaw [Fig. 7(b)]. Meanwhile, Paxson station data indicated a deep snow cover close to 1-m thick in March, the snow depth was still more than 40 cm by April end, and the snow still lasted in May [Fig. 7(c)]. Paxson mean daily temperatures started to reach above freezing toward the end of April. Note that the temperature records at the three stations all showed

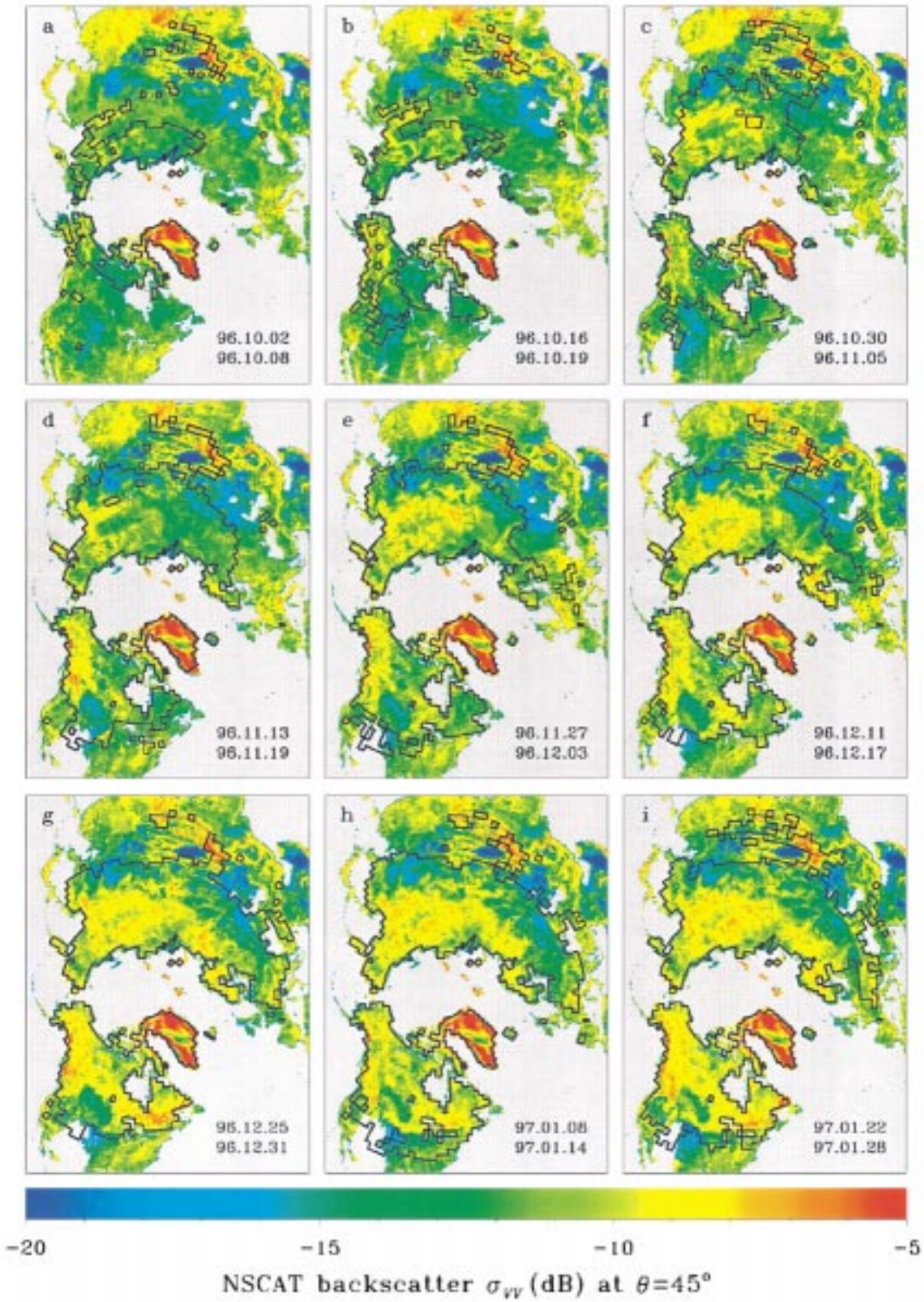

Fig. 5. (a)–(i) Time-series of NSCAT images over snow covered regions with NOAA/NESDIS and CPC snow extent contours during the snow season from October 1996 to June 1997.

the warm spell in first half of April; however, the absolute temperatures was colder and snow was still covering the northern and the southern regions of Alaska.

As seen in the NSCAT image in Fig. 6(a), Umiat was located in the high (yellow-orange) areas, Fairbanks was in the low (green) backscatter region, and Paxson was on a relative

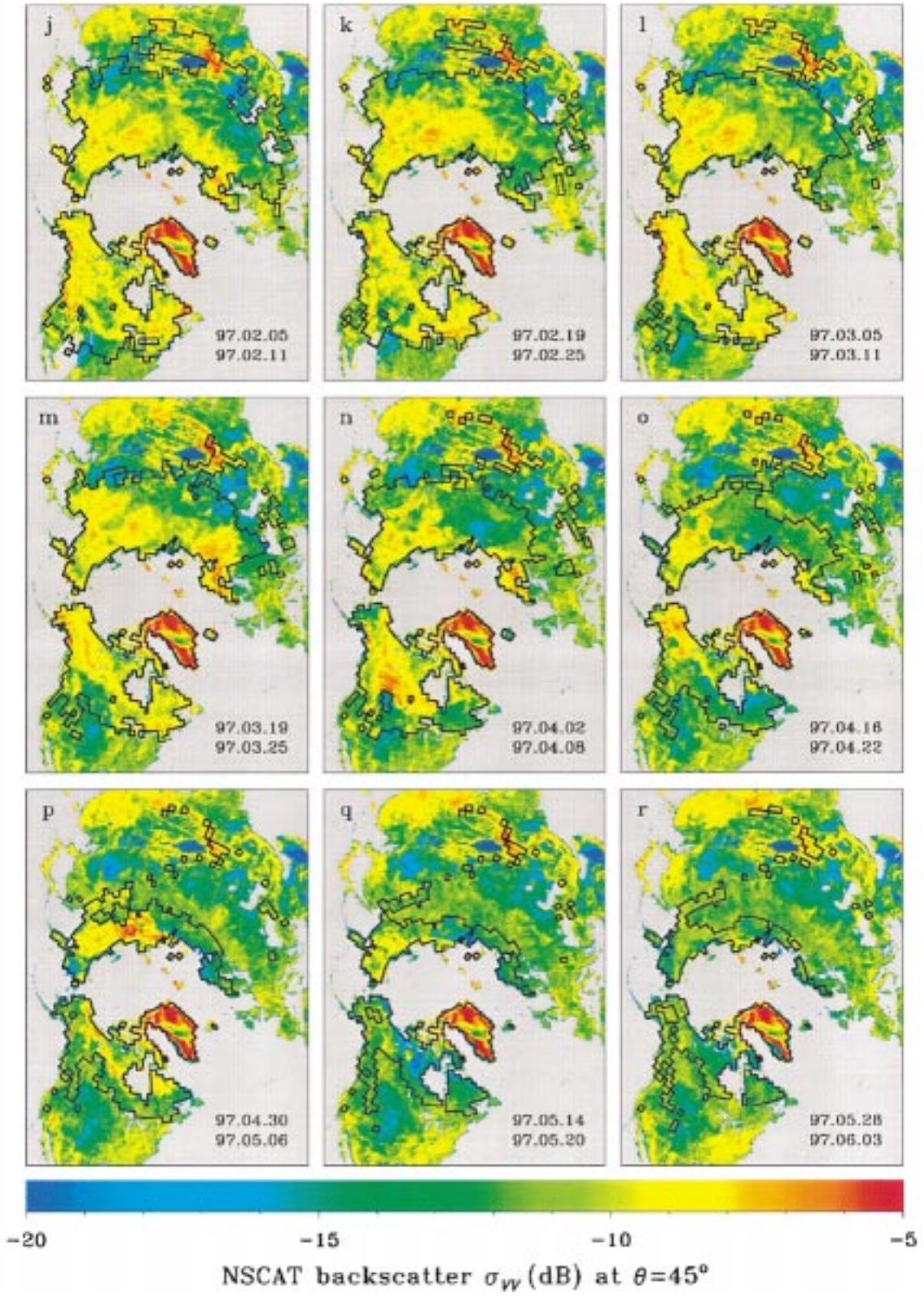

Fig. 5. (*Continued.*) (j)–(r) Time-series of NSCAT images over snow covered regions with NOAA/NESDIS and CPC snow extent contours during the snow season from October 1996 to June 1997.

high backscatter strip corresponding the the high local topographic relief. Thus, weather station observations agree with NSCAT backscatter pattern, which indicates an earlier snow departure in central Alaska. Note that this pattern was not observable from the NOAA snow extent results well later into May [Figs. 5(q)–(r)].

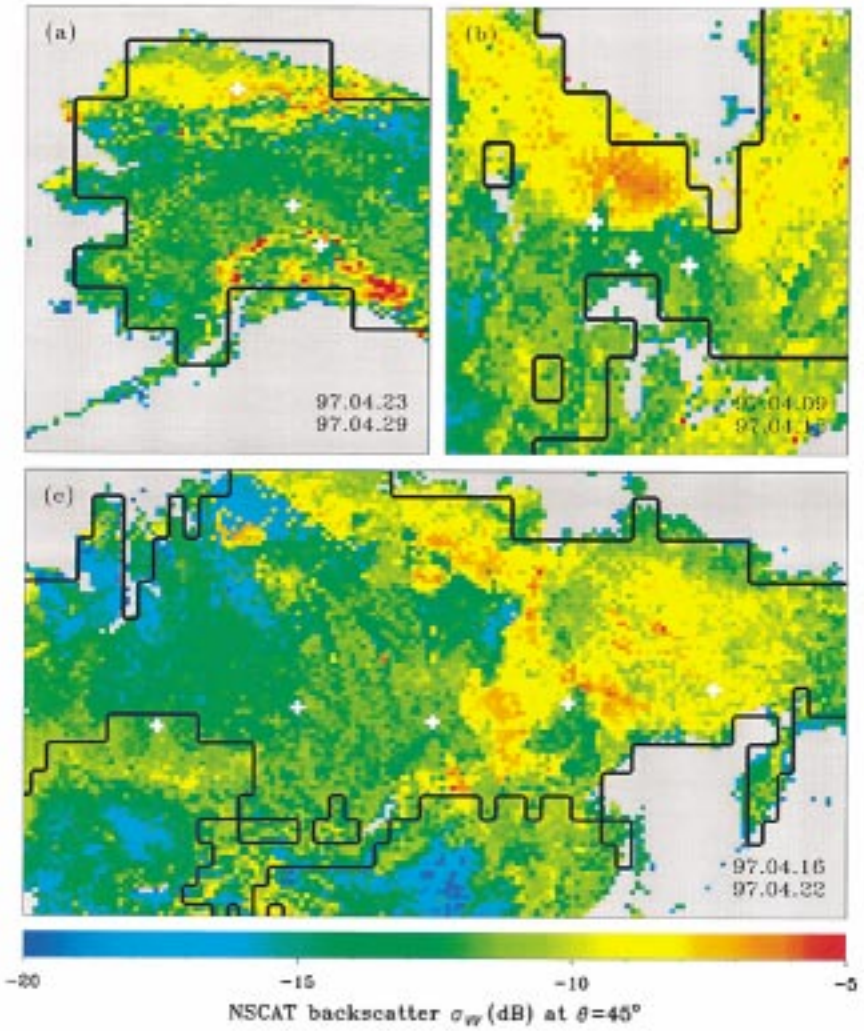

Fig. 6. NSCAT backscatter signature over snow cover regions with *in-situ* stations marked by white plusses in: (a) Alaska mapped with Mercator projection over 52° N 72° N and 137° W 169° W with stations at Umiat, Fairbanks, and Paxson from north to south, (b) Ontario mapped with Mercator projection over 40° N 60° N and 70° W 102° W with stations at Pickle Lake, Geraldton, and Kapuskasing for west to east, and (c) Siberia mapped with Mercator projection over 44° N 74° N and 60° E 170° E with stations at Aleksandrovskoe, Bajkit, Lensk, Curapka, and Sejmcan from west to east. The black contour lines represent snow extents determined by the NOAA/NESDIS and CPC product.

B. Ontario

In Ontario, Canada, the higher NSCAT backscatter signature shown in Fig. 6(b) had retreated much to the north during April 9 to April 15, 1997, while the NOAA snow extent was covering to latitudes well below the Great Lakes. Then, the backscatter retreat continued furthermore during April and May 1997. To compare this pattern with *in-situ* measurements, we use three different stations spanning across Ontario at latitudes around 50° N. From the west to the east, the stations are Pickle Lake located at 51° 28'N and 90° 12'W at an altitude of 386 m, Geraldton at 49° 47'N and 86° 56'W at 351 m, and Kapuskasing at 49° 25'N and 82° 28'W at 227 m.

Snow depth and temperature data are plotted in Figs. 8(a)–(d) for Kapuskasing, Geraldton, and Pickle Lake stations, respectively. In Fig. 8, the vertical lines denote the time period corresponding to data acquisition time of the NSCAT image in Fig. 6(b). Similar to the general trend of seasonal snow observed in Alaska, all three stations in Ontario revealed the gradual increase of snow depth from the beginning of the snow season and the rapid snowmelt at the end. At Kapuskasing station, the maximum snow depth in March was close to 2 m. During the NSCAT observation time shown in Fig. 6(b), snow depth was reduced by one order of magnitude as seen in Fig. 8(a) in response to the corresponding melting temperatures [Fig. 8(b)–(d)]. By the end of the NSCAT observation time in Fig. 6(b), snow depth at Pickle Lake decrease to about 25 cm while snow at Geraldton and Kapuskasing melted down to a much thinner depth. Corresponding to this spatial pattern of snow distribution, Fig. 6(b) shows that Pickle Lake station was located at the edge of a high (yellow) backscatter area while the backscatter at Geraldton and Kapuskasing was in the low value (green) region.

Note a pronounced warming period was observed in early April from the Kapuskasing temperature record similar to the case in Alaska. The same trend was also evident at both Geraldton and Pickle Lake stations, where the rapid snowmelt started with the early April warming event was observed in the *in-situ* data. The trend of the rapid snowmelt in April, with the fast dynamic change revealed by NSCAT backscatter, is well

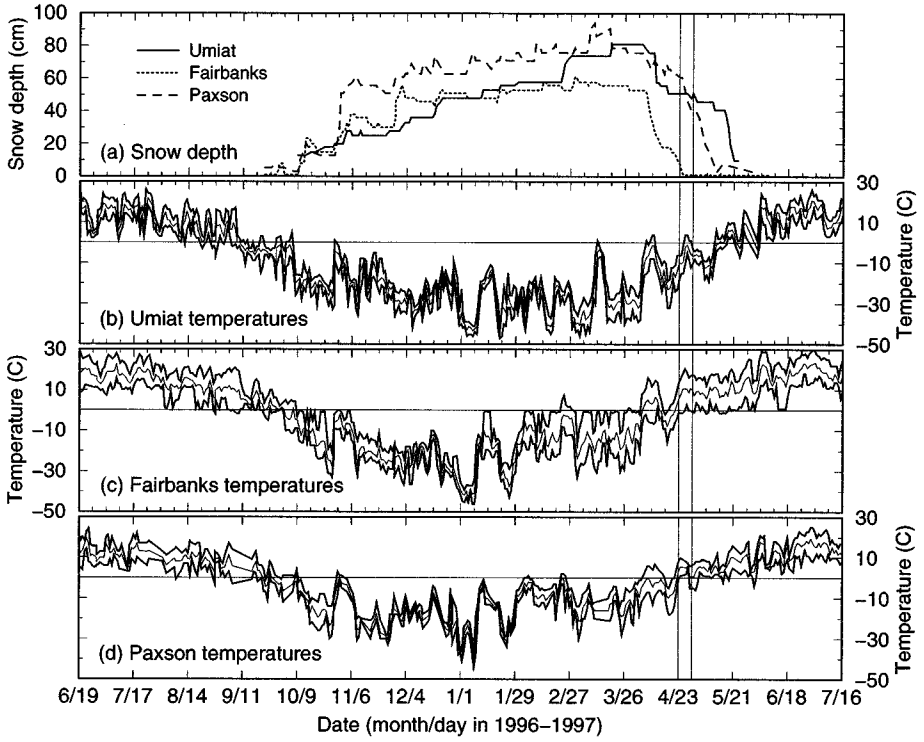

Fig. 7. *In-situ* measurements at weather stations in Alaska: (a) snow depth in centimeters, (b) temperature in degrees Celsius at Umiat, (c) temperature in degrees Celsius at Fairbanks, (d) temperature in degrees Celsius at Paxson.

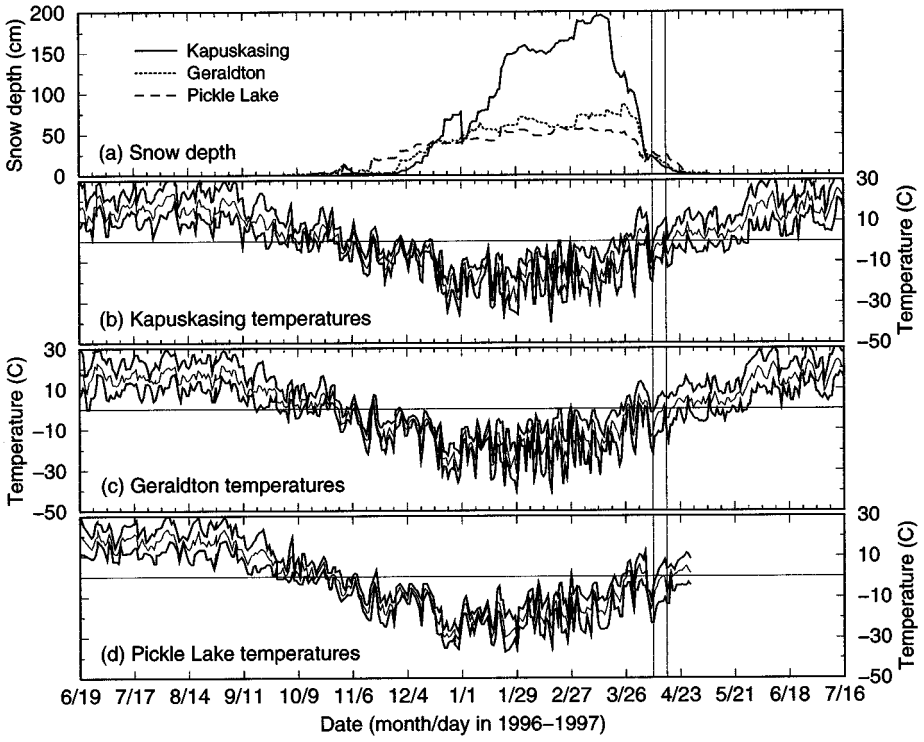

Fig. 8. *In-situ* measurements at weather stations in Ontario: (a) snow depth in centimeters, (b) temperature in degrees Celsius at Kapuskasing, (c) temperature in degrees Celsius at Geraldton, and (d) temperature in degrees Celsius at Pickle Lake.

correlated with the *in-situ* melting temperatures measured by all three stations at the same time period.

The consistency of the rapid retreat pattern in NSCAT backscatter signature, observed not only on the regional scale but across the north American continent, seems to confirm the temperature correlation, marked by the April warming event, measured by various weather stations separated by thousands of kilometers between Alaska and Ontario. Due to the large

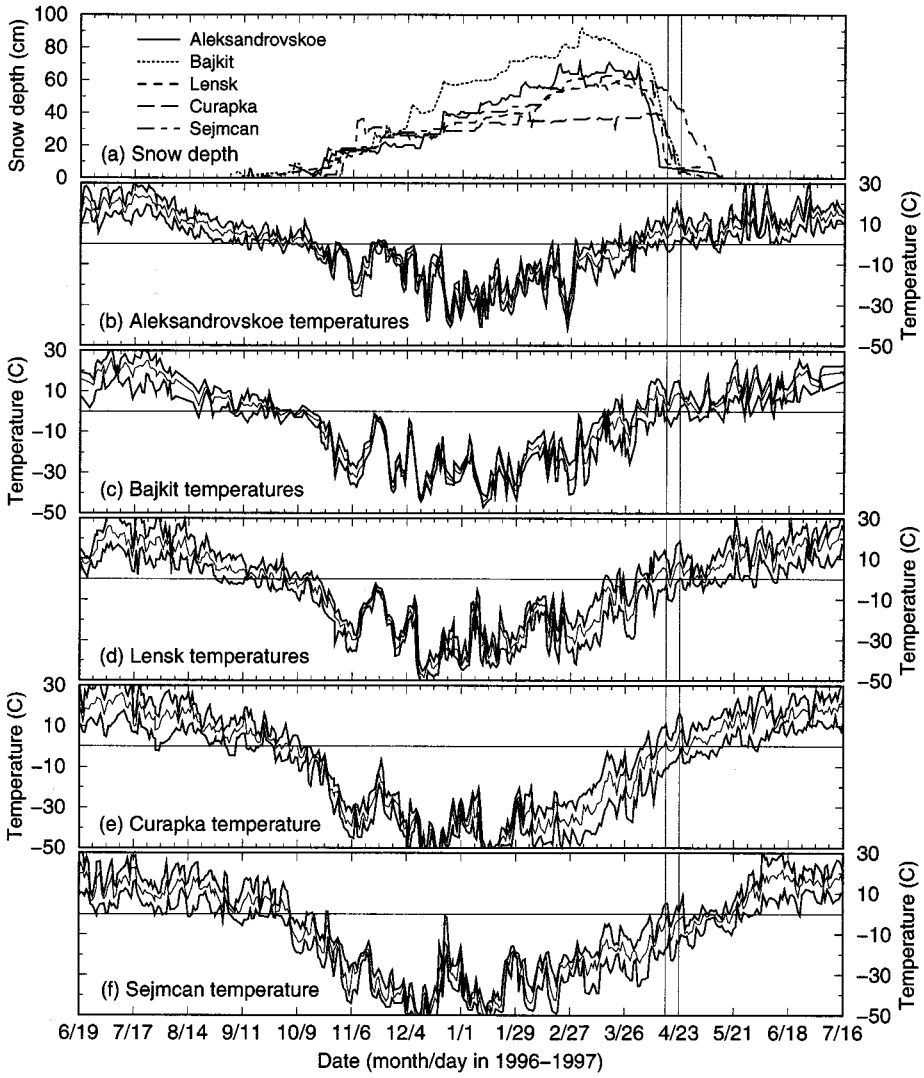

Fig. 9. *In-situ* measurements at weather stations in Siberia: (a) snow depth in centimeters, (b) temperature in degrees Celsius at Aleksandrovskoe, (c) temperature in degrees Celsius at Bajkit, (d) temperature in degrees Celsius at Lensk, (e) temperature in degree Celsius at Curapka, and (f) temperature in degree Celsius at Sejmcan.

coverage of NSCAT, the scatterometer data is valuable as an integrated indicator of large-scale climate conditions compared to local point measurements by the global weather station network.

C. Siberia

NSCAT backscatter signature over the northern hemispheric snow cover regions in Figs. 5(m)–(o) shows an interesting mirror symmetry between Eurasia and North America across the longitudinal line coincident with the international Date Line. Here, we examine the case of the retreat in NSCAT pattern corresponding to Fig. 5(o) (April 16 to April 22, 1997) over Siberia where the NOAA snow extent still indicated an extensive coverage. NSCAT backscatter over this region is plotted again to show more details in Fig. 6(c), where the weather stations are also marked on the map. Fig. 6(c) shows that the high backscatter pattern reduced to the Magadan region in east Siberia in April, compared to the strong backscatter pattern over the entire Siberia by the end of March.

Five different stations extending from the east of the Ob River, through central Siberia, to Magadan region in the far east of Siberia are selected for this study. All located around latitude 61° N and separated approximately by 19° in longitude, the weather stations are Aleksandrovskoe (60° 26'N, 77° 52'E, altitude 47 m), Bajkit (61° 40'N, 96° 22'E, 261 m), Lensk (60° 43'N, 114°53'E, 243 m), Curapka (62° 02'N, 132° 36'E, 179 m), and Sejmcan (62° 55'N, 152° 25'E, 207m). *In-situ* snow depth and temperature data from these stations are presented in Fig. 9(a)–(f), where the vertical lines indicate the NSCAT observation time of Fig. 6(c).

Four stations at Aleksandrovskoe, Bajkit, Lensk, and Curapka had shallow snow depths (< 8 cm) by the period of the NSCAT observation in Fig. 6(c). The snow became rapidly thinner and snow depths were reduced by one order of magnitude toward the end of April compared to those at the beginning of April as seen at the four stations in Fig. 9(a). From the corresponding temperature records shown in Fig. 9(b)–(e),

the fast snowmelt was caused by the April strong warming starting at the beginning of the month.

This trend is well correlated to the backscatter retreat pattern observed in Fig. 6(c). The NSCAT image shows that Aleksandrovskoe, Bajkit, and Lensk stations were all in the low (green) backscatter region. Compared with the NOAA snow extent, only Aleksandrovskoe was right below the snow extent line while the other stations were well within the snow cover. For the case at Curapka, NSCAT backscatter signature indicates that the station was located near the northern side of a distinctively low backscatter area surrounded by higher backscatter patterns [Fig. 6(c)].

At Sejmcan station in Magadan, the temperature plot in Fig. 9(f) indicates that the first part of April was still below freezing and the maximum temperature increased over freezing with a cold period in the middle of the later half part of April. Correspondingly, the snow depth at Sejmcan was still around 42 cm by the end of the period of the NSCAT image in Fig. 6(c), where the backscatter pattern was still relatively strong over the Sejmcan region in agreement with the station observations.

VI. The 1997 Flood of the Century

The high sensitivity of K_u-band backscatter to snow properties, especially snowmelting, as examined together with *in-situ* station data in the last section, enables the use of the backscatter signature over snow covered areas as an early indicator of fast snowmelt conditions leading to flood events. We illustrate the utility of wideswath scatterometer with large and frequent coverage for such practical applications with the event of the 1997 Flood of the Century occurred while NSCAT was in operation.

A. The Disaster

Numerous heavy snow storms in a long winter accounted for this disaster, according to NOAA National Climatic Data Center [13]. An early April blizzard dumped up to three feet of snow in parts of the Northern Plains and the snowmelting made river level forecasting more difficult. On April 17, 1997, the Red River broke the 100 year flood crest record at Fargo, North Dakota. Many lives were lost and costs were estimated in the $1–2 billion range in the Grand Forks area alone. North Dakota's Devils Lake expanded to more than twice its normal size and set a new record for its highest level. The Minnesota River also caused a great deal of damage [13].

The Federal Emergency Management Agency (FEMA) also reported that North Dakota and Minnesota experienced flooding due to heavy spring snowmelts [46]. North Dakota, South Dakota, and Minnesota were declared federal disasters [47]. The American Red Cross provided numerous shelters, food, and other critically-needed assistance to thousands of families evacuated from towns such as Grand Forks, North Dakota, and East Grand Forks, Minnesota [48]. Upon departing to North Dakota, President Clinton made remarks on a town being flooded and burning at the same time and a large community being entirely evacuated [49]. In the Province of Manitoba, Canada, the flood inflicted severe and extensive damages, a state of emergency was declared in southern Manitoba on April 22, 1997, and close to 4000 soldiers were deployed south of Winnipeg to help the battle against the flood [50].

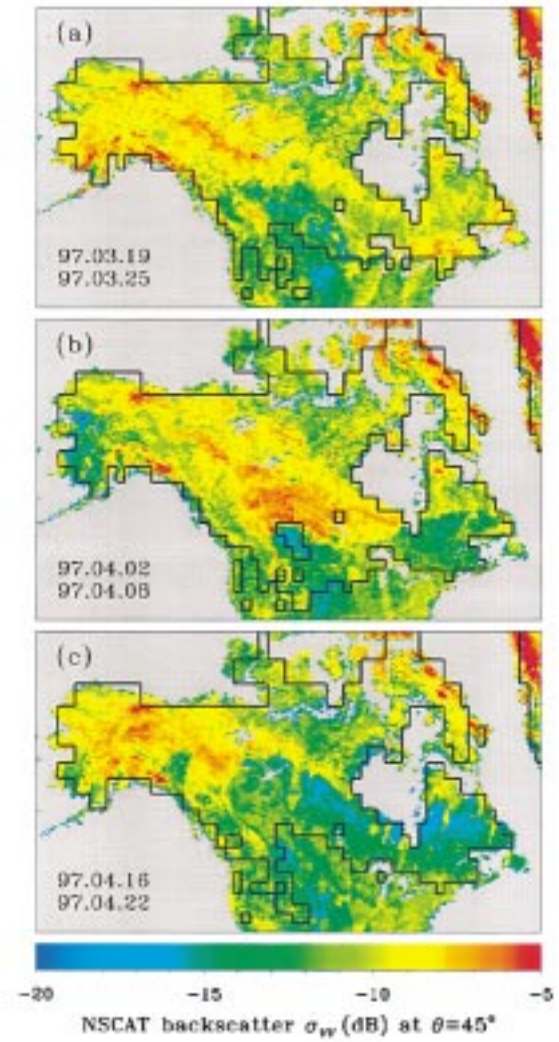

Fig. 10. NSCAT backscatter signatures over snow cover corresponding to snow events leading to the 1997 Flood of the Century in the U.S. north plains and the Canadian prairie region: (a) period of snowmelt from 97–03-19 to 97–03-25, (b) period of snow blizzard from 97–04-02 to 97–04-08, and (c) period of rapid snow retreat from 97–04-16 to 97–04-22.

B. NSCAT Observations

NSCAT backscatter images are obtained to investigate the backscatter signature over the snow cover leading to the 1997 Flood of the Century. Fig. 10(a)–(c) present NSCAT results together with the corresponding NOAA/NESDIS and CPC snow extent contour over north America.

Fig. 10(a) shows the case for the week of March 19 to March 25, 1997. This period was in the spring seasonal transition. Strong backscatter patterns were still observed in mid-latitude areas such as the Great Lakes region in the east and the high topography region in the west. However, over the northern plains and prairie region in the middle of the north American continent, the yellow strong backscatter response had retreated further north compared to the east and west sides. The retreat observed in the NSCAT backscatter signature was more pronounced than that seen in the snow extent contour. Note that a

drop of 3 dB (decrease by a factor of 2) in backscatter changes the backscatter color code from yellow to green. As discussed in Section II-E, a small percentage wetness in snow can cause such a change in K_u-band backscatter resulting in a more pronounced retreat pattern seen in NSCAT data.

A dramatic change is evident in the NSCAT image in Fig. 10(b) over an extensive region between the U.S. midwest and Canada. The time period in early April 1997 for the case of Fig. 10(b) corresponds to the time of the blizzard dumping several feet of snow as presented in the above section. Fig. 10(b) shows very strong backscatter, appeared as orange to red, right over the previous green backscatter region where the strong yellow backscatter had retreated northward two-week earlier as seen in Fig. 9(a). Such high backscatter area in the north plains and prairie regions shown in Fig. 9(b) was extending even further south in latitudes compared to the southern extension of the yellow backscatter pattern in Quebec, Labrador, and Newfoundland in the east of Canada. Note that a small low blue backscatter area coincides with a no-snow contour area located to the west of North Dakota.

From April 16 to April 22, 1997, NSCAT data in Fig. 10(c) reveal a rapid retreat of the high backscatter pattern to high latitudes up into the middle region of the Northwest Territories. This backscatter pattern is well above the NOAA/NESDIS and CPC snow contour line. Examinations of later NSCAT backscatter time-series data sets in April to May [see Fig. 5(p)–(q)] indicate that the retreat continued to the north afterward. Such rapid retreat of the NSCAT pattern suggest a rapid melt of snow in the first part of April leading to the flood. Note that the time periods of these events are consistent with the NOAA report of the 100-year flood record of the Red River at Fargo (see Section VI.A). With much more pronounced and dynamic patterns compared to the snow extent contour, NSCAT backscatter dramatically exhibited the series of snow events causing the devastating 1997 Flood of the Century. With this experience, a similar set of scatterometer observations in the future is likely a considerable predicator of severe flooding.

VII. Summary and Conclusions

The objective of this paper is to show the potential of wideswath K_u-band scatterometry for applications to snow remote sensing on the regional to continental and global scales. From the snow scattering physics together with published radar measurements of snow, we present that K_u-band backscatter is sensitive to snow properties.

Using NSCAT data, we show for the first time that global K_u-band backscatter signature in snow-covered regions reveals patterns corresponding to different global snow classes defined by the CRREL snow classification system. Such observations hold over regions with different vegetation types and forest areas during the snow season. This is an indication of the sensitivity of K_u-band scatterometer observations to snow physical characteristics on the global scale.

Examinations of the entire NSCAT backscatter data all over the northern hemisphere throughout the 1996–1997 snow season within the NOAA/NESDIS and CPC snow-covered extent show the characteristics trend of the seasonal snow backscatter evolution. The backscatter started with a low-value pattern, increased during the season as snow accumulated, and rapidly decreased by the end of the season corresponding to the fast snowmelt process. Furthermore, NSCAT backscatter within the northern hemispheric snow extent exhibits more details and rapid changes corresponding to the distributions and dynamics of the global snow cover.

The comparison of global NSCAT backscatter data with *in-situ* snow depth and temperature data obtained from the global weather station network over three different and important snow-covered regions of the world, including Alaska in U.S., Ontario in Canada, and Siberia in Russia, shows the close correlation of the NSCAT backscatter retreat patterns with the snowmelt process observed at various weather stations. These results further indicate the sensitivity of K_u-band scatterometer is sufficient for snow monitoring.

To illustrate the practical utility of wideswath K_u-band scatterometer as an early indicator of large-scale snowmelt causing floods, we investigate NSCAT backscatter signature corresponding to the snow events leading to the 1997 Flood of the Century over the U.S. northern plains and the Canadian prairie region. NSCAT backscatter shows dramatic changes with pronounced and dynamic patterns correlated with the April blizzard and rapid snowmelt causing the devastating flood.

Nevertheless, there are certainly limitations in NSCAT data. First, the use of NSCAT subswath data effectively narrows down the total NSCAT swath. Moreover, the total swath of NSCAT may not be large enough to begin with. Consequently, the temporal resolution of the global coverage is limited to weekly observations. This may not adequate to capture the dynamics of the global snow cover during transient snow events or rapid snowmelt processes. For example, a well-defined green patch of backscatter is seen within the surrounding yellow pattern in the southern area between Alaska and Canada in Fig. 5(o). This is caused by data overlaid from different orbits in the one-week time scale, during which properties of snow covered had changed.

Another limitation of NSCAT is the variation in incidence angles, which introduces more uncertainties in the backscatter observations due to the data interpolation to a constant incidence angle. The interpolation also results in a higher cost because multiple measurements at different incidence angles are necessary for each location. Furthermore, as a characteristics of the global-coverage class of sensors, NSCAT resolution was approximately 7 km $\times$ 25 km, which needs to be improved for monitoring regions of patchy snow cover. Also because of the single frequency system, NSCAT data have difficulties in observing very thin or very thick snow. A multifrequency scatterometer system is better for snow monitoring; however, such a system is costly. Combining with other global-coverage sensors such as AVHRR or SSM/I will provide a more comprehensive data set for global snow applications.

With the past NSCAT data, this paper shows the potential use of the scatterometer for global snow remote sensing. In June 1999, the SeaWinds K_u-band scatterometer on the QuikSCAT satellite was successfully launched by a Titan II rocket from the Vandenberg Air Force Base in California. The SeaWinds

scatterometer currently collects global backscatter data with a fixed incidence angle over a very wideswath of 1800 km. Such coverage can provide daily data over 37° latitude, where almost all global snow covered regions are located. At higher latitudes (above 40°), QuikSCAT/SeaWinds can even provide twice daily coverage allowing diurnal monitoring of global snow. Furthermore, another SeaWinds scatterometer is planned to be launched in 2002 will provide long-term time-series data.

With potential applications to snow and global data sets extending into the new millennium, it is pertinent to develop scatterometry algorithms for quantitative snow cover monitoring. Such efforts require better understanding of K_{u}-band scattering mechanisms in relation to snow physical processes and determining more accurate quantitative relationship between backscatter and snow physical parameters.

In this regard, the Jet Prolusion Laboratory has successfully developed and implemented a tower-based polarimetric K_{u}-band scatterometer system designed for operations in cold regions for snow measurements [51]. Using this new scatterometer system, JPL and CRREL carried a snow field experiment in Alaska in March–April 1999 to investigate backscatter signature of snow during the late phase of the snow season [52]. We have applied the experimental results to develop initial algorithms to derive snow extent and snowmelt-freeze regions from QuikSCAT data [53]. Results will be validated with snow field experimental observations to be presented in future papers.

It is recognized that much research work needs to be done to develop geophysical model functions relating backscatter to geophysical properties of different snow classes for developing appropriate snow algorithms using scatterometer data. Nevertheless, the past, current, and future scatterometers serve as opportune test beds providing real global data sets for the development of scatterometry remote sensing of snow from space.

ACKNOWLEDGMENT

The authors thank D. Garrett of the NOAA Climate Prediction Center for the NOAA/NESDIS and CPC snow extent product. In particular, the authors thank M. Sturm for the global snow class data and insightful discussions with him on snow properties.

REFERENCES

[1] D. A. Robinson and G. Kukla, "Maximum surface albedo of seasonally snow covered lands in the northern hemisphere," *J. Climate Appl. Meteorol.*, vol. 24, pp. 402–411, 1985.

[2] J. L. Foster and A. T. C. Chang, "Snow cover," in *Atlas of Satellite Observations Related to Global Change*, R. J. Gurney, C. L. Parkinson, and J. L. Foster, Eds. Cambridge, U.K.: Univ. Cambridge Press, 1993, pp. 361–370.

[3] P. Y. Groisman, T. R. Karl, R. W. Knight, and G. L. Stenchikov, "Changes of snow cover, temperature, and radiative heat balance over the Northern Hemisphere," *J. Climate*, vol. 7, no. 11, pp. 1633–1656, 1994.

[4] M. Matson, D. R. Wiesnet, C. P. Berg, and E. P. McClain, "New data and new products: The NOAA/NESS continental snow-cover data base," in *Proc. 4th Annu. Climatology Workshop*, Madison, WI, Oct. 16–18, 1979, pp. 351–364.

[5] K. F. Dewey and R. Heim Jr, "Satellite Observations of Variations in Northern Hemisphere Seasonal Snow Cover," NOAA Tech. Rep. NESS 87, U.S. Dept. Commerce, Washington, DC, 1981.

[6] J. E. Walsh, "Operational satellites and the global monitoring of snow and ice," *Global Planetary Change*, vol. 90, no. 1-3, pp. 219–224, 1991.

[7] R. D. Cess, G. L. Potter, M.-H. Zhang, J.-P. Blanchet, S. Chalita, R. Colman, D. A. Dazlich, A. D. D. Genio, V. Dymnikov, V. Galin, D. Jerrett, E. Keup, A. A. Lacis, H. L. Truet, X.-Z. Liang, J.-F. Mahfouf, B. J. McAvaney, V. P. Meleshko, J. F. B. Mitchell, J.-J. Morcrette, P. M. Norris, D. A. Randall, L. Rikus, E. Roeckner, J.-F. Royer, U. Schlese, D. A. Sheinin, J. M. Slingo, A. P. Sokolov, K. E. Taylor, W. M. Washington, R. T. Wetherrald, and I. Yagai, "Interpretation of snow-climate feedback as produced by 17 general circulation models," *Science*, vol. 253, no. 5022, pp. 888–892, 1991.

[8] C. Schutz and L. D. Bregman, "Global Annual Snow Accumulation by Months," Rand Note N-2687-RC Pub., Rand Corp., Santa Monica, CA, 1988.

[9] D. J. Foster and R. D. Davey, "Global snow depth climatology," U.S. Air Force Environ. Tech. Appl. Center, Scott Air Force Base, IL, USAFETAC/TN-88/006, 1988.

[10] D. A. Robinson, K. F. Dewey, and R. R. Heim Jr, "Global snow cover monitoring: An update," *Bull. Amer. Meteorol. Soc.*, vol. 74, no. 9, pp. 1689–1696, 1993.

[11] D. K. Hall, G. A. Riggs, and V. V. Salomonson, "Development of methods for mapping global snow cover using moderate resolution imaging spectroradiometer data," *Remote Sens. Environ.*, vol. 54, no. 2, pp. 127–140, 1995.

[12] "Snow Surveys and Water Supply Forecasting," Agricul. Info. Bull., no. 536, Nat. Water Clim. Center, 1997.

[13] "The Spring of 1997, Reviewing Four Significant Weather Events," Tech. Rep., TR 97-03, Nat. Clim. Data Center, 1997.

[14] D. A. Robinson, "Evaluating snow cover over northern hemisphere lands using satellite and in situ observations," in *Proc. 53rd Annu. Eastern Snow Conf.*, Williamsburg, VA, May 2–3, 1996, pp. 13–19.

[15] A. Basist, D. Garrett, R. Ferraro, N. Grody, and K. Mitchell, "A comparison between snow cover products derived from visible and microwave satellite observations," *J. Appl. Meteorol.*, vol. 35, no. 2, pp. 163–177, 1996.

[16] M. Matson and D. R. Weisnet, "New data base for climate studies," *Nature*, vol. 289, pp. 451–456, 1981.

[17] D. R. Weisnet and M. Matson, "Monthly Winter Snowline Variation in the Northern Hemisphere From Satellite Record 1966–1975," NOAA Tech. Rep. NESS 74, Washington, DC, 1979.

[18] A. T. C. Chang, J. L. Foster, and D. K. Hall, "Nimbus-7 SMMR Derived global snow cover parameters," *Ann. Glaciol.*, vol. 9, pp. 39–44, 1987.

[19] N. Grody, "Classification of snow cover and precipitation using the special sensor microwave imager," *J. Geophys. Res.*, vol. 96, no. D4, pp. 7423–7435, 1991.

[20] S. Adam, A. Pietroniro, and M. M. Brugman, "Glacier snow line mapping using ERS-1 SAR imagery," *Remote Sens. Environ.*, vol. 61, no. 1, pp. 46–54, 1997.

[21] J. T. Koskinen, J. T. Pulliainen, and M. T. Hallikainen, "The use of ERS-1 SAR data in snow melt monitoring," *IEEE Trans. Geosci. Remote Sensing*, vol. 35, pp. 601–610, May 1997.

[22] J. Dozier, "Remote sensing of the alpine snow cover: A review of techniques and accomplishments from the visible wavelengths through the microwave," in *Int. Conf. Snow Hydrology*, J. Hardy, M Albert, and P. Marsh, Eds., Brownsville, VT, Oct 6–9, 1998, pp. 33–33.

[23] "Northern Hemisphere Snow Cover Data, Operational 89x89 Northern Hemisphere Snow Cover Data 1973–Present," NOAA/NESDIS and CPC, Washington, DC, 1999.

[24] J. A. Kong, *Electromagnetic Wave Theory*. New York: Wiley, 1986.

[25] W. H. Stiles and F. T. Ulaby, "The active and passive microwave response to snow parameters," *J. Geophys. Res.*, vol. 85, no. C2, pp. 1037–1044, 1980.

[26] C. Mätzler, "Review of radar experiments of the seasonal snow cover," *CRREL Workshop Interaction of Microwaves with the Seasonal Snow Cover*, pp. 56–56, 1984.

[27] L. Tsang and J. A. Kong, "Scattering of electromagnetic waves from random media with strong permittivity fluctuations," *Radio Sci.*, vol. 16, no. 3, pp. 303–320, 1981.

[28] S. V. Nghiem, R. Kwok, J. A. Kong, and R. T. Shin, "A model with ellipsoidal scatterers for polarimetric remote sensing of anisotropic layered media," *Radio Sci.*, vol. 28, no. 5, pp. 687–703, 1993.

[29] S. V. Nghiem, R. Kwok, S. H. Yueh, J. A. Kong, M. A. Tassoudji, C. C. Hsu, and R. T. Shin, "Polarimetric scattering from layered media with multiple species of scatterers," *Radio Sci.*, vol. 30, no. 4, pp. 835–852, 1995.

[30] F. T. Ulaby and W. H. Stiles, "The active and passive microwave response to snow parameters. 2. Water equivalent of dry snow," *J. Geophys. Res.*, vol. 85, no. C2, pp. 1045–1049, 1980.
[31] W.-Y. Tsai, J. E. Graf, C. Winn, J. N. Huddleston, S. Dunbar, M. H. Freilich, F. J. Wentz, D. G. Long, and W. L. Jones, "Postlaunch sensor verification and calibration of the nasa scatterometer," *IEEE Trans. Geosci. Remote Sensing*, vol. 37, pp. 1517–1542, May 1999.
[32] W.-Y. Tsai, C. Winn, J. Huddleston, B. Stiles, M. Spencer, S. Dunbar, and S. V. Nghiem, "Seawinds on QuikSCAT: Overview of sensor system and post-launch calibration/verification," in *Proc. Prog. Electromagnetics Research Symp.*, Cambridge, MA, July 5–14, 2000.
[33] J. S. Sperry, K. L. Nichols, J. E. M. Sullivan, and S. E. Eastlack, "Xylem embolism in ring-porous, diffuse-porous, and coniferous trees of northern Utah and interior Alaska," *Ecology*, vol. 75, no. 6, pp. 1736–1752, 1994.
[34] F. Magnani and M. Borghetti, "Interpretation of seasonal changes of xylem embolism and plant hydraulic resistance in fagus-sylvatica," *Plant Cell Environ.*, vol. 18, no. 6, pp. 689–696, 1995.
[35] T. S. Feild and T. Brodribb, "Stem water transport and freeze-thaw xylem embolism in conifers and angiosperms in a Tasmanian treeline heath," *Oecologia*, vol. 127, no. 3, pp. 314–320, 2001.
[36] S. V. Nghiem, M. Borgeaud, J. A. Kong, and R. T. Shin, "Polarimetric remote sensing of geophysical media with layer random medium model," in *Progress in Electromagnetics Research*, J. A. Kong, Ed, New York: Elsevier, 1990, vol. 3, pp. 1–73.
[37] S. V. Nghiem, T. L. Toan, J. A. Kong, H. C. Han, and M. Borgeaud, "Layer model with random spheroidal scatterers for remote sensing of vegetation canopy," *J. Electromagn. Waves Appl.*, vol. 7, no. 1, pp. 49–76, 1993.
[38] S. V. Nghiem, R. Kwok, S. H. Yueh, and M. R. Drinkwater, "Polarimetric signatures of sea ice," *J. Geophys. Res.*, vol. 100, no. C7, pp. 13 665–13 679, 1995.
[39] S. V. Nghiem, K. Steffen, R. Kwok, and W.-Y. Tsai, "Detection of snow melt regions on the Greenland ice sheet using diurnal backscatter change," *J. Glaciol.*, to be published.
[40] V. Wismann, "Monitoring of seasonal thawing in siberia with ERS scatterometer data," *IEEE Trans. Geosci. Remote Sensing*, vol. 38, pp. 1804–1809, July 2000.
[41] M. Sturm, J. Holmgren, and G. E. Liston, "A seasonal snow cover classification system for local to global applications," *J. Climatol.*, vol. 8, no. 5, pp. 1261–1283, 1995.
[42] W. L. Allen, Ed., "Nat. Geographic," in *Atlas of the World*. Washington, D.C: Nat. Geogr. Soc, 1995.
[43] R. D. West, W.-Y. Tsai, J. L. Granger, and W. H. Daffer, "Calibration of the nasa scatterometer using a ground calibration station," in *Proc. SPIE*, vol. 3439, W. L. Barnes, Ed., San Diego, CA, July 19–21, 1998, pp. 450–459.
[44] D. Garrett, Personal communication, 1998.
[45] "Global Surface Summary of the Day Data," Nat. Clim. Data center, Federal Climate Complex, 1998.
[46] "Upper Midwest Floods Situation Rep.," FEMA, Washington, DC, 1997.
[47] "Upper midwest flood update," FEMA, Washington, DC, 1997.
[48] "American red cross launches flood relief campaign: $18 million sought to assist flood victims," *American Red Cross, Disaster News*, Apr. 1997.
[49] "Remarks by the president and vice president upon departure," The South Lawn, 9:05 A.M. EDT, The White House, Washington, DC, Apr. 22, 1997.
[50] "Federal government assistance to victims of the manitoba floods," Manitoba Emergency Management Org., Apr. 30, 1997.
[51] S. V. Nghiem, "K_u-band polarimetric scatterometer," JPL Tech. Rep., Adv. Radar Tech. Prog, Jet Propul. Lab., Pasadena, CA, 1999.
[52] S. V. Nghiem, M. Sturm, D. K. Perovich, B. Taras, B. Elder, and W.-Y. Tsai, "Alaska snow experiment for applications of scatterometry to snow remote sensing," in *AGU Fall Meeting*, San Francisco, CA, Dec. 1999.
[53] S. V. Nghiem, W.-Y. Tsai, G. Neumann, M. Sturm, D. K. Perovich, B. Taras, and B. Elder, "Global snow signatures in K_u-band backscatter," in *Proc. Int. Geoscience and Remote Sensing Symp.*, Honolulu, HI, July 24-28, 2000.

Son V. Nghiem received the B.S. in electrical engineering (summa cum laude) from Texas A&M University, College Station, in 1985, and the S.M. and Ph.D. degrees from the Department of Electrical Engineering and Computer Science, Massachusetts Institute of Technology, Cambridge, in 1988 and 1991.

In 1991, he joined the Jet Propulsion Laboratory, California Institute of Technology, Pasadena. His research encompasses active and passive remote sensing techniques, instrumentation and experimentation, electromagnetic wave theory and applications, and modeling of the geophysical environment.

Dr. Nghiem received the 1999 Lew Allen Award of Excellence for his research on polarimetric scatterometry for earth science remote sensing and for contributions to future spaceborne advanced instrument concepts. He is a member of the American Geophysical Union, the Scientific Research Society of Sigma Xi, and the Honor Society of Phi Kappa Phi.

Wu-Yang Tsai received the Ph.D. degree in theoretical physics from Harvard University, Cambridge, MA, in 1971.

He has performed research in high-energy physics, classical and quantum electrodynamics, electromagnetic scattering, propagation and radiation, high-density plasma fusion, high-altitude nuclear explosion phenomenology, radiative heat transfer, synthetic aperture radar, and currently, on all aspects of scatterometer design, algorithm development, and science applications. He co-authored a graduate level text book with J. Schwinger *et al.*, *Classical Electrodynamics* (Reading, MA: Perseus Books). He is currently a Principal Engineer with the the Jet Propulsion Laboratory, California Institute of Technology, Pasadena, and is the Project Engineer of SeaWinds on QuikSCAT (QSCAT), SeaWinds on ADEOS-2 (SeaWinds), and many advanced scatterometer projects. He is also the Group Supervisor of the Scatterometer System Engineering Group.